Dalton Transactions

Accepted Manuscript

ROYAL SOCIETY OF CHEMISTRY

www.rsc.org/dalton

Journal Name

RSCPublishing

ARTICLE

Facile electrochemical synthesis of CeO_2@Ag@CdS nanotube arrays with enhanced photoelectrochemical water splitting performance

Cite this: DOI: 10.1039/x0xx00000x

Received 00th January 2012,
Accepted 00th January 2012

DOI: 10.1039/x0xx00000x

www.rsc.org/

Mi Zhao,[a,o] Haohua Li,[b,o] Xiaoping Shen,*[a] Zhenyuan Ji, [a] and Keqiang Xu [a]

In this work, for the first time, three-component CeO_2@Ag@CdS heterostructured nanotube arrays with remarkable photoelectrochemical (PEC) performance have been synthesized by electrodeposition method. In this configuration, the modification with Ag nanoparticles can significantly strengthen the light absorption and provide an interior direct pathway to facilitate the separation and transport of photogenerated carriers. Therefore, the CeO_2@Ag@CdS heterostructured nanotubes generate a remarkable photocurrent density of 2.14 mA cm^{-2} at potential of −0.2 V (*vs*. Ag/AgCl), which is 9.8 and 2.4 times higher than that of two-component CeO_2@Ag system (0.218 mA cm^{-2}) and CeO_2@CdS system (0.879 mA cm^{-2}), respectively. It also gives efficiency as high as 69% around 360 nm in the incident photon to electron conversion efficiency (IPCE) spectrum. Moreover, the stability of photoelectrode was tested over 16 min. Furthermore, these results provide a valuable insight for the further development of such materials for PEC water splitting.

Introduction

Photoelectrochemical (PEC) water splitting using semiconductor metal oxides has gained great interest owing to the large-scale production of hydrogen with sustainable sunlight without yielding carbon dioxide.[1-6] Rare earth oxides have been widely used in the PEC system as the photoelectrode due to their outstanding optical characteristics and carrier transportation capability.[7-9] As a typical rare earth oxide, CeO_2 has been utilized as a photoanode in PEC water splitting.[10-12] However, the performance of CeO_2 photoanode is limited by its wide bandgap (3.2 eV), which makes CeO_2 capture only ultraviolet irradiation (about 4% of solar energy).[10] Therefore, the development of highly efficient CeO_2 nanostructures with good light-harvesting capability is of great importance for the improvement of the PEC performance.[13,14]

Recently, the construction of a heterojunction between transition metal oxides and suitable narrow bandgap semiconductors has been demonstrated as a promising and effective solution to improve the light-harvesting capability and suppress the electron-hole recombination.[15-20] For example, Tong *et al*. have demonstrated the enhanced photocatalytic performance of the CeO_2@CdS heterostructured spheres due to its type-II heterostructure.[20] However, the efficiency of photogenerated carriers transportation has been limited due to the interfacial effects between two different materials.[21-23]

On the other hand, noble metal nanoparticles such as Ag, Au and Pt *etc*. have been extensively deposited on the surface of various metal oxides for enhancing PEC performance.[24-26] Because plasmonic noble metal nanoparticles can act as photosensitizers to strengthen the optical absorption of metal-semiconductor composite systems.[27-29] Moreover, the junctions formed between the semiconductor and noble metal nanoparticles can facilitate the separation of photogenerated charge carriers, thereby improving the efficiency of PEC conversion.[30,31] For example, Ag nanoparticles anchored at CeO_2 are beneficial for enhancing PEC performance owing to decreasing the recombination of carriers and extending the response of CeO_2 to visible light.[24] Therefore, it is expected that the PEC performance can be further enhanced by incorporating both narrow bandgap semiconductors and noble metal nanoparticles into metal oxides to form three-component heterostructures. However, such three-component systems based CeO_2 are seldom reported so far due to the large synthesis challenge.

Here, we report for the first time the synthesis of three-component CeO_2@Ag@CdS nanotube arrays (NTAs) on FTO substrate by an effective electrodeposition method, which combines the heterostructure formation and noble metal modification to further improve the PEC performance. The essence of our design is schematically illustrated in Fig. 1. In this three-component system, Ag nanoparticles have two important functions. Firstly, they act as photosensitizers, which can improve the absorption in visible light and enhance the absorption intensity through the localized surface

plasma resonance (LSPR) effect.[32,33] Secondly, they can sever as carrier conductors, which can provide an interior direct pathway to facilitate the photoinduced carriers transportation at interface between CeO_2 and CdS.[22] It is demonstrated that the three-component CeO_2@Ag@CdS nanotubes show significantly enhanced PEC performance as compared with the pristine CeO_2 nanotubes and two-component (CeO_2@Ag or CeO_2@CdS) systems.

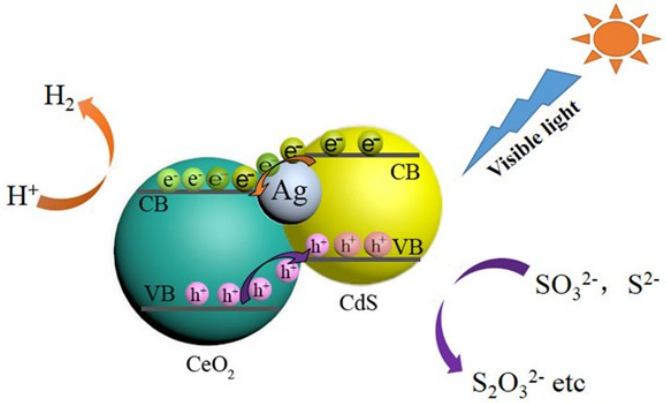

Fig. 1 The diagram for band alignment of the CeO2@Ag@CdS heterostructure nanotubes.

Experimental

Materials

All chemicals used in this study are analytical reagent and were used without further purification. The used substrates are fluorine-doped SnO_2 (FTO) coated glass purchased from Wuhan lattice solar energy technology Co., LTD.

Synthesis of CeO_2, CeO_2@Ag, CeO_2@CdS and CeO_2@Ag@CdS NTAs

The electrodeposition was carried out in a conventional three-electrode electrochemical cell using a home-made HDV-7C potentiostatic apparatus with a cathodic electrodeposition method. The reference electrode and the counter electrode are a saturated Ag/AgCl electrode and a graphite rod of about 4.0 cm^{-2}, respectively. The working electrode is an F-doped SnO_2-coated glass (FTO, 1 cm × 2 cm) with a sheet resistance of 14 Ω cm^{-2}. Prior to electrodeposition, the FTO glass was cleaned ultrasonically in distilled water, ethanol, and acetone and then rinsed in distilled water again.

The fabrication of the CeO_2@Ag@CdS NTAs involves three steps, as illustrated in Scheme 1. Firstly, CeO_2 NTAs were electrodeposited on FTO substrates in a 25 mL solution of 0.01 M $Ce(NO_3)_3$ and 30% DMSO (30 vol % DMSO: 70 vol % H_2O) with a current potential of -1.1 V (*vs* Ag/AgCl) for 40 min at 90 °C. After the reaction, the substrate was removed from the reactor, washed with deionized water and dried. Secondly, to obtain the CeO_2@Ag nanocomposites, the Ag nanoparticles were deposited on the surface of CeO_2 NTAs through a successive electrodeposition in a solution of 0.5 mM $AgNO_3$ at a current density of 0.1 mA cm^{-2} at room temperature for 8 min. Finally, CdS layer was at last deposited and covered on the CeO_2@Ag system to form three-component CeO_2@Ag@CdS nanocomposites, which were performed in a solution of 0.01 M $Cd(NO_3)_3$ and 0.01 M thiourea at a current density of 0.35 mA cm^{-2} for 10 min at 90 °C. In addition, The CeO_2@CdS heterostructures were formed by using the obtained CeO_2 nanotubes as working electrode and in a solution of 0.01M $Cd(NO_3)_3$ and 0.01M thiourea with a current density of 0.35 mA cm^{-2} at 90 °C for 10 min.

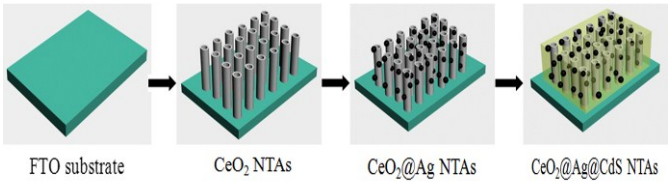

Scheme 1 Synthetic route to the CeO_2@Ag@CdS heterostructured NTAs.

Characterizations

The as-synthesized products were characterized using X-ray diffraction (XRD, D8 ADVANCE), field emission scanning electron microscopy (FE-SEM, Hitachi, S-4800), transmission electron microscopy (TEM, JEM2100-HR) and X-ray energy dispersive spectroscopy (EDS, INCA-Oxford). The optical properties of the samples were measured with a UV-vis spectrophotometer (UV, Shimadzu UV-2450) and a combined fluorescence time and steady state spectrometer (PL, Varian Cary Eclipse).

Photoelectrochemical measurements

The PEC tests were performed in a conventional three-electrode single compartment quartz cell. 0.43 M Na_2S and 0.5 M Na_2SO_3 were preferentially used as the electroyte in PEC measurements, while 0.5 M Na_2SO_4 was used as electroyte in IPCE measurements. The saturated calomel electrode and the platinum wire electrode are employed as reference and counter electrode, respectively. The working electrodes are the FTO with CeO_2@Ag@CdS thin films with a light irradiation area of 1.0 cm^{-2}. The illumination source is a 300 W Xe lamp (PLS-SXE300 (UV), Perfect light Technology Co., Ltd. Beijing) and a monochromator (Newport) was used to investigate wavelength-dependent photocurrent, and the output intensity of the light source was measured with the same radiometer (Merlin). The distance between the light and solution was fixed to be 25 cm. The PEC tests were carried out on a CHI 760D electrochemical analyzer (ChenHua Instruments, Shanghai, China). The potential was swept from −1.4 to 0.2 V (*vs*.Ag/AgCl) with a sweep rate of 20 mV s^{-1}. The photocurrent density *vs*. time was measured at a potential of −0.2 V (*vs*. Ag/AgCl). The incident photon to electron conversion efficiency (IPCE) of the samples was calculated as follows:

$$IPCE = (1240I)/(\lambda J_{light})$$

Where I is the photocurrent density (mA cm^{-2}), λ the incident light wavelength (nm), and J_{light} is the incident light intensity (mW cm^{-2}).

Results and discussion

Characterization of CeO_2, CeO_2@Ag, CeO_2@CdS and CeO_2@Ag@CdS NTAs

The crystal phases of obtained samples were first determined by XRD (Fig. 2). As shown in Fig. 2, the diffraction peaks of CeO_2 are consistent with the fluorite cubic structure of CeO_2 (a = 5.404 Å, JCPDF no.65-5923), while the CdS coating are consistent with the hexagonal structure of CdS (a =4.141 Å, JCPDF no. 65-2887). However, the peaks of the Ag nanoparticles are not observed due to the small mass loading and uniform distribution, which could be investigated by EDS (Fig. S1) and TEM thereinafter. In addition, The amount of Ag and CdS deposited on the electrodes were tested using EDX analysis,[34] and the results are shown in Fig. S1. No other diffraction peaks were detected besides SnO_2 peaks that come from the FTO substrates, revealing the high purity of the as-synthesized products.

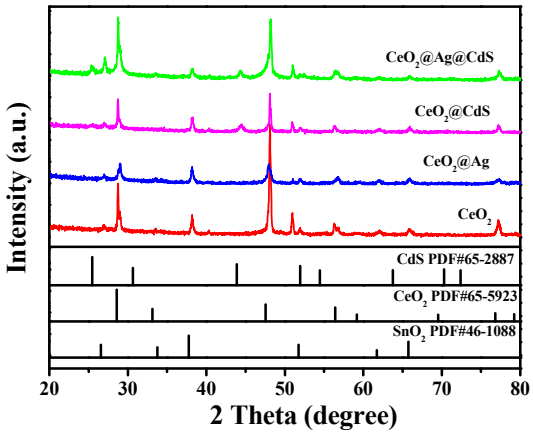

Fig. 2 XRD patterns of as-prepared CeO_2, CeO_2@Ag, CeO_2@CdS and CeO_2@Ag/CdS.

The detailed morphology, size and microstructure of the obtained samples were then observed by SEM (Fig. 3). Fig. 3a shows the well-aligned CeO_2 nanotubes were successfully synthesized on the surface of FTO substrates. The more detailed view of the CeO_2 nanotubes is shown in Fig. 3b, the average diameter of CeO_2 nanotubes is about 150 nm and the wall thickness is about 30 nm. And the cross-sectional SEM image of the CeO_2 NTAs is given in Fig. 3c, it can be seen that the length of the well-ordered nanotubes is about 2 μm. In addition, it also shows that there are a large number of stacking gaps among these nanotubes, which are beneficial for material modification. The surface morphology of CeO_2@Ag is shown in Fig. 3d. The surface of the CeO_2 NTAs is rather rough since it is covered with a number of Ag nanoparticles. Similarly, in Fig. 3e, it can be seen that the CeO_2@CdS nanotubes are thicker than CeO_2 nanotubes, implying that CdS layer was successfully deposited on the surface of CeO_2 nanotubes. In Fig. 3f, it is noteworthy that there are almost no gaps in the CeO_2 nanotubes, suggesting that the CeO_2@Ag system is sheathed by a CdS layer. Thus, it could be concluded that the CeO_2, CeO_2@Ag, CeO_2@CdS and CeO_2@Ag@CdS NTAs were successfully grown on the FTO substrates.

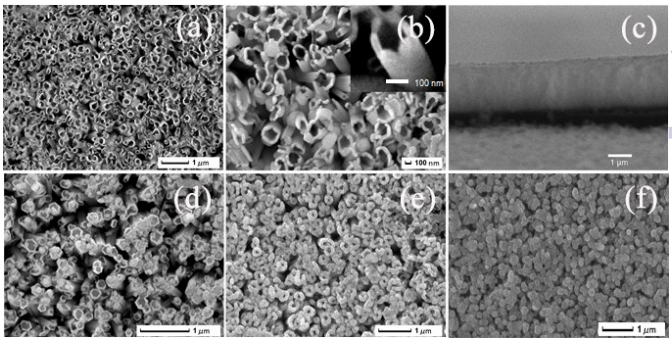

Fig. 3 SEM images of as-synthesized (a-b) CeO_2. (c) Cross-section image of CeO_2. (d) CeO_2@Ag. (e) CeO_2@CdS and (f) CeO_2@Ag@CdS nanotubes

Ag peaks in XRD pattens cannot be observed due to the small mass loading, and so more microstructure details of the CeO_2@Ag and CeO_2@Ag@CdS nanotube were further investigated by TEM and HRTEM (Fig. 4). A low-magnification TEM image of CeO_2@Ag nanotube is illustrated in Fig. 4a, it can be seen that the Ag nanoparticles are anchored on the surface of CeO_2 nanotube with a particle size of 36 nm. Fig. 4b,c are HRTEM images of the square region from Fig. 4a. The lattice fringes with a d-spacing of 0.238 nm correspond to the (111) planes of the cubic phase Ag (JCPDF no. 65-8428). The lattice fringes with d-spacing of 0.311 nm correspond to the (111) lattice plane of the fluorite cubic CeO_2 (JCPDF no. 65-5923). Fig. 4d is the TEM image of CeO_2@Ag@CdS nanotube, it is evidence that the surface of CeO_2@Ag is coated with a thin layer of CdS. The HRTEM images of the square region in Fig. 4d is shown in Fig. 4e,f, it can be clearly seen

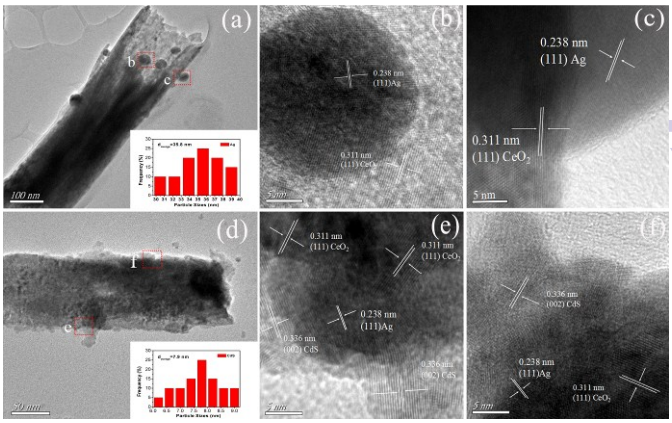

Fig. 4 (a) TEM and (b,c) HRTEM images of CeO_2@Ag; (d) TEM and (e,f) HRTEM images of CeO_2@Ag@CdS. The insets in (a) and (d) show the size distributions of Ag nanoparticles and CdS layers, respectively.

that the interfaces between CeO_2, Ag and CdS in the three-component heterostructure. In Fig. 4e,f the lattice fringes with d-spacing of 0.311 nm correspond to the (111) planes of the fluorite cubic CeO_2 (JCPDF no. 65-5923). The clear lattice spacing of 0.238 nm belongs to the lattice fringes of the (111) plane of the cubic phase Ag, while the lattice fringes with a d-

spacing of 0.335 nm correspond to the (002) lattice plane of the hexagonal CdS (JCPDF no. 65-2887). Hence, based on the results above, the CeO_2, CeO_2@Ag, CeO_2@CdS and CeO_2@Ag@CdS NTAs were successfully fabricated on the FTO substrates.

Photoelectrochemical performance

Furthermore, the PEC performance of the deposited films (CeO_2, CeO_2@Ag, CeO_2@CdS and CeO_2@Ag/CdS) was investigated by the linear sweep voltammograms (Fig. 5a) and time-dependent photocurrent (Fig. 5b). As shown in Fig. 5a, the linear sweep voltammograms of these samples reveal three remarkable differences in PEC performance. Firstly, under irradiation, the photocurrent density of the CeO_2@Ag@CdS NTAs is 2.14 mA cm^{-2}, which is substantially higher than those of CeO_2 (0.138 mA cm^{-2}), CeO_2@Ag (0.218 mA cm^{-2}) and CeO_2@CdS (0.879 mA cm^{-2}) at the same applied potential of

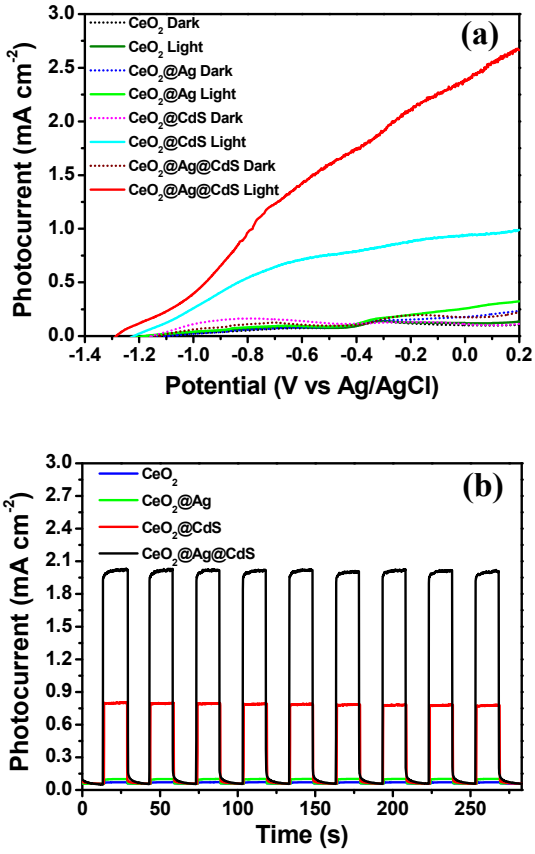

Fig. 5 (a) Linear sweep voltammograms curves for the photocurrent response of the CeO_2, CeO_2@Ag, CeO_2@CdS and CeO_2@Ag@CdS photoelectrodes in dark and under visible light irradiation. (b) The time-dependent photocurrent curves of the CeO_2, CeO_2@Ag, CeO_2@CdS and CeO_2@Ag@CdS photoelectrodes under illumination of visible light.

−0.2 V (*vs*. Ag/AgCl). Similarly, the same trend can also be seen in Fig. 5b. As shown in Fig. 5b, upon irradiation, it is clearly shown that the transient photocurrent density of the CeO_2@Ag@CdS nanotubes is 2.02 mA cm^{-2}, which is 15.5, 9.8 and 2.4 times higher than those of CeO_2, CeO_2@Ag, CeO_2@CdS at the same applied potential of −0.2 V (*vs*. Ag/AgCl), respectively. In other words, the photocurrent densities follow this order: CeO_2@Ag@CdS > CeO_2@CdS > CeO_2@Ag > CeO_2. The higher photocurrent density means that more photoinduced electrons have been transferred from the CeO_2@Ag@CdS nanotubes to the counter electrode via external circuit. Secondly, the onset potential of the CeO_2@Ag@CdS NTAs distinctively shifted to the negative direction compared to others samples. This apparent negative shift of onset potential suggests that the Fermi energy level of the three-component heterostructure has been elevated.[35] The onset potential increases in this order: CeO_2@Ag@CdS < CeO_2@CdS < CeO_2@Ag < CeO_2. Thirdly, there is no observed saturation of photocurrent density through the whole potential scan range for the CeO_2@Ag@CdS heterostructure system in contrast to the photocurrent density of the other three samples being saturated at 0.2 V (*vs*. Ag/AgCl), implying a more efficient charge separation in the three-component heterostructure.[22] Taken together, the PEC performance follows this order: CeO_2@Ag@CdS > CeO_2@CdS > CeO_2@Ag > CeO_2 and these results provide explicit evidences that the three-component CeO_2@Ag@CdS heterostructured NTAs are beneficial for an increase of photoelectrons and significantly effective charge separation.

Another important performance for the PEC cells application is the chemical stability of the photoelectrode.[36,37] Fig. 6a shows photocurrent stability (*vs*. time curve) of the CeO_2, CeO_2@Ag, CeO_2@CdS and CeO_2@Ag@CdS nanotubes at −0.2 V (*vs*. Ag/AgCl). The photocurrent decays quickly for the CeO_2@Ag nanotubes photoelectrodes. In contrast, the CeO_2@Ag@CdS nanotubes keep photostability, probably the Ag nanoparticles were coated with CdS layers. The CeO_2, CeO_2@CdS and CeO_2@Ag@CdS NTAs show improved photostability under continuous illumination for more than 16 min. Moreover, in order to comprehensively investigate the stability of different samples in PEC measurement, we performed the cyclic voltammograms (CVs)[38] of different samples in dark and light irradiation and XRD and SEM characterization of different samples before and after PEC measurement (Fig. S2-4). Taken together, it demonstrates that the CeO_2, CeO_2@CdS and CeO_2@Ag@CdS photoelectrodes exhibit excellent photoability in electrolytes(S^{2-}, SO_3^{2-}).

In order to make a quantitative correlation between all the samples, we performed IPCE measurements as a means of studying the photoactive wavelength regime for the deposited films (CeO_2, CeO_2@Ag, CeO_2@CdS and CeO_2@Ag/CdS) (Fig. 6b).[39,40] As shown in Fig. 6d, the deposited films were assessed at wavelengths ranging from 300 to 700 nm at −0.2 V (*vs*. Ag/AgCl) in 0.5 M Na_2SO_4. Compared of these samples, the CeO_2@Ag@CdS gives the highest efficiency. The CeO_2@Ag@CdS NTAs achieve an IPCE of 69% at 360 nm, which is 3.21, 2.13, 1.65 times higher than those of CeO_2, CeO_2@Ag, CeO_2@CdS at the same applied potential of −0.2 V (*vs*. Ag/AgCl), respectively. Compared the IPCE of CeO_2@Ag@CdS NTAs with previously reported CdS based electrodes, the CeO_2@Ag@CdS electrodes give higher efficiency.

[1,41] The results are consistent with the linear sweep voltammograms. Moreover, the CeO_2@CdS and CeO_2@Ag@CdS NTAs show substantial photoactivity in the visible light region from 350 to 520 nm in addition to strong photoresponse in the near-UV. In conclusion, the observed enhanced photocurrent density of the three-component CeO_2@Ag@CdS NTAs, which combines the hetero-structure formation and noble metal modification could be ascribed to the enhanced light absorption and charge carrier transfer.

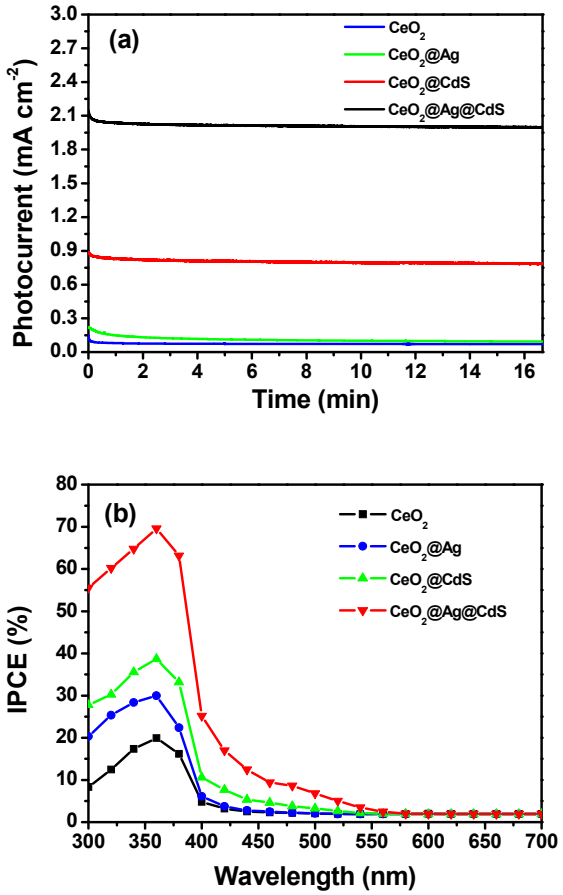

Fig. 6 (a) Chronoamperometric time-dependent photocurrent curves of CeO_2, CeO_2@Ag, CeO_2@CdS and CeO_2@Ag@CdS photo-electrodes measured at −0.2 *vs* Ag/AgCl for 16.7 min. (b) Dependence of the IPCE on the incident wavelength of different electrodes at −0.2 (vs Ag/AgCl).

The mechanism of PEC performance

Considering the above results, a schematic diagram is illustrates in Fig. 7 to understand the mechanism of PEC performance with the obtained photoelectrodes. The mechanism of photoelectrodes were identified according to the previous reports. [1,14,20,22,39] Compared to CeO_2@CdS nantubes, the three-component CeO_2@Ag@CdS hetero-structured nanotubes are beneficial for increasing photoelectrons and effective charge separation due to the Ag nanoparticles at the interface of CeO_2@CdS. The Ag nanoparticles in the three-component system have two important functions. Firstly, they act as photosensitizers, which can improve the absorption in visible light and enhance the absorption intensity through the LSPR effect.[32,33] Secondly, they can sever as carrier conductors, which can provide an interior direct pathway to facilitate the separation and transport of photogenerated carriers at interface of type-II heterostructures.[22] This mechanism is also suitable for CeO_2@Ag and CeO_2, and thus the PEC performance of CeO_2@Ag nanotubes is distinctively higher than that of CeO_2. In addition, the PEC performance of CeO_2@CdS nanotubes is obviously higher than CeO_2@Ag nantubes, because the light absorption capability of narrow band-gap semiconductor shell in type-II heterostructure is substantially higher than the LSPR effect of noble metal nanoparticles at the interface of metal-semiconductor composite systems.[42]

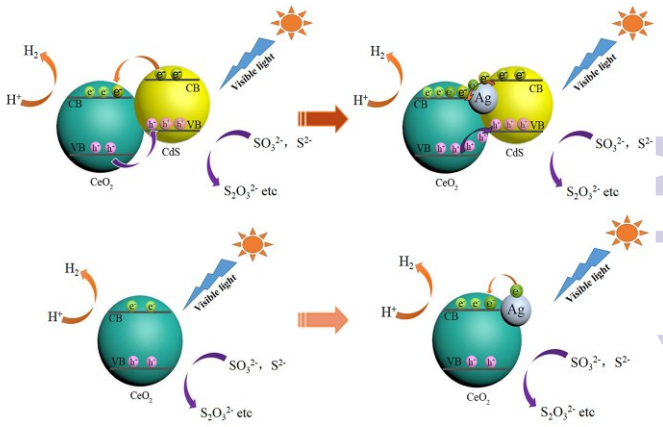

Fig. 7 PEC water splitting mechanism of the CeO_2, CeO_2@Ag, CeO_2@CdS and CeO_2@Ag@CdS heterostructured nanotubes.

Optical properties of CeO_2, CeO_2@Ag, CeO_2@CdS and CeO_2@Ag@CdS NTAs

To understand the mechanism for the improved PEC performance, the optical properties of the samples were characterized by UV-vis absorption spectra (Fig. 8a). By analyzing the data, we can conclude two important conclusions. Firstly, it is generally believed that the light absorption capability of narrow band-gap semiconductor shell in type-II staggered band alignment is substantially higher than the LSPR effect of noble metal nanoparticles at the interface of metal-semiconductor composite systems.[42] Indeed, our experimental observations further confirm this conclusion. As shown in Fig. 8a, in contrast to the CeO_2@Ag nanotubes, CeO_2@CdS nanotubes exhibit a noticeable increase in light absorption intensity and a remarkable red shift of the bandgap. Secondly, it is widely accepted that the noble metal nanoparticles act as photosensitizers, which can improve the absorption in visible light and enhance the absorption intensity through the LSPR effect.[32,33,43] This trend was also observed in our experiments. As shown in Fig. 8a, the absorption intensity of CeO_2@Ag@CdS NTAs is obviously higher than CeO_2@CdS nanotubes. Similarly, this is also suitable for CeO_2@Ag and CeO_2. Therefore, CeO_2@Ag nanotubes have higher absorption intensity than CeO_2 ones. Thus, we can infer that Ag nanoparticles in the composites are highly effective for improving the light absorption ability.

Moreover, the enhanced photoexcited charge separation efficiency could be further verified by photoluminescence (PL)

spectroscopy (Fig. 8b). It is generally believed that the noble metal nanoparticles act as carrier conductors, which can provide an interior direct pathway to facilitate the separation and transport of photogenerated carriers at interface of type-II heterostructures, resulting in the quenching effect of PL intensity.[22] Indeed, our experimental observations are in excellent agreement with this

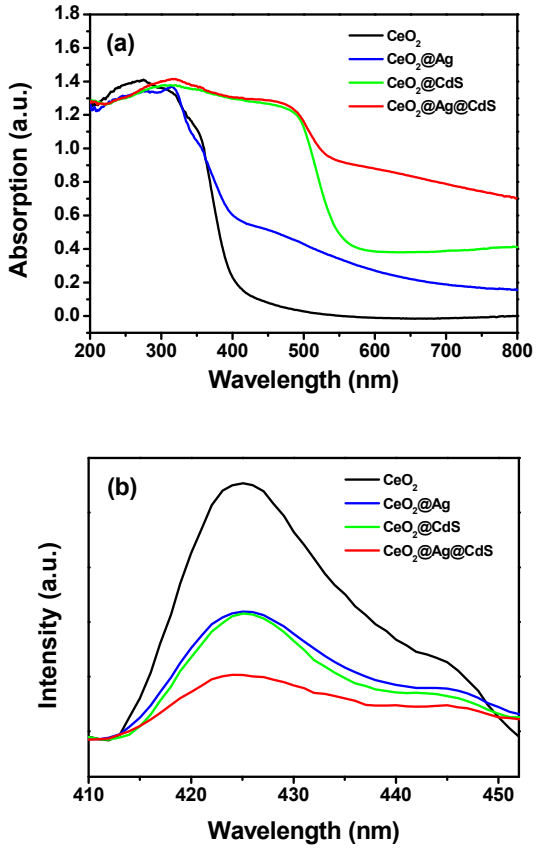

Fig. 8 (a) UV-Vis absorption spectra of CeO_2, CeO_2@Ag, CeO_2@CdS and CeO_2@Ag@CdS nanotubes. (b) Room-temperature PL spectra of CeO_2, CeO_2@Ag, CeO_2@CdS and CeO_2@Ag@CdS nanotubes collected at the excitation wavelength of 270 nm.

conclusion. As shown in Fig. 8b, the emission intensity of CeO_2@Ag@CdS nanotubes at 425 nm is much lower than CeO_2@CdS nanotubes, which can effectively suppress the recombination of carriers. This trend is also suitable for CeO_2@Ag and CeO_2. Compared to CeO_2 nanotubes, the CeO_2@Ag nanotubes have lower emission intensity. However, the emission intensity of CeO_2@CdS and CeO_2@Ag is nearly at the same level, the detailed mechanism requires further study. Therefore, we can conclude that the drastic quenching of the emission clearly indicates the construction of the CeO_2@Ag@CdS heterostructures is reasonable and can effectively suppress the recombination of charges. Taken as a whole, the enhanced PEC properties of CeO_2@Ag@CdS heterostructures are direct consequence of the synergetic effects of enhanced visible light absorption and effective the separation and transportation of photogenerated carriers at interface of type-II heterostructure via the Ag nanoparticles, which is consistent with our hypothesis (Fig. 1).

Conclusions

In summary, the three-component CeO_2@Ag@CdS hetero-structured NTAs exhibit enhanced PEC properties due to the synergetic effects of enhanced visible light absorption and effective separation and transportation of photogenerated carriers at interface of type-II heterostructure via the Ag nanoparticles. The CeO_2@Ag@CdS heterostructured nano-tubes generate a remarkable photocurrent density of 2.14 mA cm^{-2} at potential of −0.2 V (*vs*. Ag/AgCl), which is 2.4 times higher than that of two-component CeO_2@CdS systems (0.879 mA cm^{-2}). It also gives efficiency as high as 69% around 360 nm in the IPCE spectrum. The results demonstrate that the CeO_2@Ag@CdS heterostructured nanotubes are a promising material for use as a photoanode for PEC water splitting. Moreover, noble metal loading at type-II heterostructure also opened a promising avenue for the rational design and fabrication of high efficiency heterostructured functional materials.

Acknowledgements

The authors are grateful for financial support from National Nature Science Foundation of China (No. 51272094, 51302111) and Specialized Research Fund for the Doctoral Program of Higher Education of China (No. 20123227110018).

Notes and references

[a] School of Chemistry and Chemical Engineering, Jiangsu University, Zhenjiang 212013, P. R. China, Fax: (+86)511-88791800; Tel: (+86)511-88791800; E-mail: xiaopingshen@163.com
[b] School of Material Science and Engineering, Jiangsu University, Zhenjiang 212003, P. R. China
[O] These authors contributed equally to this work.

1 J. Zhang, L. H. Wang, X. H. Liu, X. A. Li and W. Huang, *J. Mater. Chem. A,* 2015, **3**, 535.
2 J. Qi, K. Zhao, G. D. Li, Y. Gao, H. J. Zhao, R. B. Yu and Z. Y. Tang, *Nanoscale*, 2014, **6**, 4072.
3 S. W. Cao and J. G. Yu, *J. Phys. Chem. Lett.*, 2014, **5**, 2101.
4 H. M. Chen, C. K. Chen, R. S. Liu, L. Zhang, J. J. Zhang and D. P. Wilkinson, *Chem. Soc. Rev.,* 2012, **41**, 5654.
5 M. T. Mayer, J. Lin, G. Yuan and D. Wang, *Acc. Chem. Res.*, 2014, **46**, 1558.
6 G. M. Wang, X. H. Lu, T. Zhai, Y. C. Ling, H. Y. Wang, Y. X. Tong and Y. Li, *Nanoscale*, 2012, **4**, 3123.
7 D. Prieto-Centurion, T. R. Eaton, C. A. Roberts, P. T. Fanson, J. M. Notestein, *Appl. Catal. B* 2015,**168-169**, 68.
8 P. Sheng, W. Li, J. Cai, X. Tong, Q. Cai and C. A. Grimes, *J. Mater. Chem. A*, 2013, **1**, 7806.
9 H. M. Zhu, N. H. Song and T. Q. Lian, *J. Am. Chem. Soc.*, 2010, **132**, 15038.
10 C. Zhang, X. Y. Zhang, Y. C. Wang, S. L. Xie, Y. Liu, X. H. Lu and Y. X. Tong, *New J.Chem.*, 2014, **38**, 2581.
11 X. H. Lu, T. Zhai, H. N. Cui, J. Y. Shi, S. L. Xie, Y. Y. Huang, C. L. Liang and Y. X. Tong, *J. Mater. Chem*., 2011, **21**, 5569.

12 H. Yu, Y. Bai, X. Zong, F. Tang, G. M. Lu and L. Wang, *Chem. Commun.*, 2012, **48**, 7386.
13 W. Li, S. L. Xie, M. Y. Li, X. W. Ouyang, G. F. Cui, X. H. Lu and Y. X. Tong, *J. Mater. Chem. A*, 2013, **1**, 4190.
14 J. Zhang, L. Li, X. Huang and G. Li, *J. Mater. Chem.*, 2012, **22**, 10480.
15 C. Z. Yao, B. H. Wei, L. X. Meng, H. Li, Q. J. Gong, H. Sun, H. X. Ma and X. H. Hu, *J. Power Sources*, 2012, **207**, 222.
16 S. L. Xie, X. H. Lu, T. Zhai, J. Y. Gan, W. Li, M. Xu, M. H. Yu, Y. M. Zhang and Y. X. Tong, *Langmuir*, 2012, **28**, 10558.
17 Y. Xie, Z. B. Yu, G. Liu, X. L. Ma and H. M. *Cheng, Energy Environ. Sci.*, 2014, **7**, 1895.
18 K. E. deKrafft, C. Wang and W. B. Lin, *Adv.Mater.*, 2012, **24**, 2014.
19 H. H. Li, C. Chen, X. Y. Huang, Y. Leng, M. N. Hou, X. G. Xiao, J. Bao, J. L. You, W. W. Zhang, Y. K. Wang, J. Song, Y. P. Wang, Q. Q. Liu and G. A. Hope, *J. Power Sources*, 2014, **247**, 915.
20 X. H. Lu, S. L. Xie, T. Zhai, Y. F. Zhao, P. Zhang, Y. L. Zhang and Y. X. Tong, *RSC. Adv.*, 2011, **1**, 1207.
21 S. L. Xie, T. Zhai, Y. J. Zhu, W. Li, R. L. Qiu, Y. X. Tong and X. H. Lu, *Int. J. Hydrogen Energy*, 2014, **39**, 4820.
22 Y. Hou, F. Zuo, A. Dagg and P. Y. Feng, *Nano Lett.*, 2012, **12**, 6464.
23 R. Kobayashi, S. Tanigawa, T. Takashima, B. Ohtani and H. Irie, *J. Phys. Chem. C*, 2014, **118**, 22450.
24 M. M. Khan, S. A. Ansari, J. Lee, M. O. Ansari, J. Lee, M. H. Cho, *J. Colloid Interface Sci.*, 2014, **431**, 255.
25 M. M. Khan, S. A. Ansari, M. O. Ansari, B. K. Min, J. Lee and M. H. Cho, *J. Phys. Chem. C*, 2014, **118**, 9477.
26 N. Zhang, S. Q. Liu and Y. J. Xu, *Nanoscale*, 2012, **4**, 2227.
27 C. H. An, S. Peng and Y. G. Sun, *Adv. Mater.*, 2010, **22**, 2570.
28 C. G. Silva, R. Juarez, T. Marino, R. Molinari and H. Garcia, *J. Am. Chem. Soc.*, 2011, **133**, 595.
29 Y. Nishijima, K. Ueno, Y. Yokota, K. Murakoshi and H. Misawa, *J. Phys. Chem. Lett.*, 2010, **1**, 2031.
30 S. L. Xie, M. Y. Li, W. J. Wei, T. Zhai, P. P. Fang, R. L. Qiu, X. H. Lu and Y. X. Tong, *Nano Energy*, 2014, **10**, 313.
31 X. Q. Chen, P. Li, H. Tong, T. Kako, J. H. Ye and Sci. Technol. *Adv. Mater.*, 2011, **12**, 044604.
32 S. Linic, P. Christopher and D. B. Ingram, *Nat. Mater.*, 2011, **10**, 911.
33 R. liu, P. Wang, X. F. Wang, H. G. Yu and J. G. Yu, *J. Phys. Chem. C*, 2012, **116**, 17721.
34 Y. X. Zhu, Z. Chen, T. Gao, Q. L. Huang, F. Niu, L. S. Qin, P. Tang, Y.X. Huang, Z. L. Sha, Y. F. Wang, *Appl. Catal. B,* 2015, 163, 16.
35 J. Hensel, G. M. Wang, Y. Li and J. Z. Zhang, *Nano Lett.*, 2010, **10**, 478.
36 Y. C. Pu, Y. C. Ling, K. D. Chang, C. M. Liu, J. Z. Zhang, Y. J. Hsu and Y. Li, *J. Phys. Chem. C*, 2014, **118**, 15086.
37 Y. C. Ling, G. M. Wang, H. Y. Wang, Y. Yang and Y. Li, *ChemSusChem.*, 2014, **7**, 848.
38 X. Y. Lou, J. Y. Chen, M. D. Wang, J. L. Gu, P. Wu, D. M. Sun, Y. W. Tang, *J. Power Sources*, 2015, **287**, 203.
39 J. Miao, H. B. Yang, S. Y. Khoo, B. Liu, *Nanoscale,* 2013, **5**, 11118.
40 Y. C. Qiu, K. Y. Yan, H. Deng, S. H. Yang, *Nano Lett.,* 2012, **12**, 407.
41 Y. X. Yu, W. X. Ouyang, Z. T. Liao, B. B. Du, W. D. Zhang, *ACS Appl. Mater. Interfaces,* 2014, **6**, 8467.
42 X. L. Zhang, Y. Li, J. L. Zhao, S. G. Wang, Y. D. Li, H. T. Dai and X. W. Sun, *J. Power Sources*, 2014, **269**, 466.
43 J. S. Wu, J. S. Wang, Y. C. Du, H. Y. Li, Y. L. Yang, X. J. Jia, *Appl. Catal. B,* 2015, 174−175, 435.